PROTON ACCELERATION FROM SPHERICAL TARGETS USING HIGH INTENSITY LASER

Jubaraj Choudhury*[1], Sagar Samir Kalita[1], and Nilakshi Das[1]

[1]*Department of Physics, Tezpur University, Tezpur- 784028, Assam, India*

*Corresponding Author: jubarajchoudhury@gmail.com

(Received 25 September 2025; revised 15 December 2025; accepted 4 January 2026; published 1 August 2026)

Abstract: Laser-driven proton acceleration has emerged as an important research area, driven by its applications in medical therapy, nuclear fusion, materials science, and radiography. In this study, we explore spherical targets as proton sources, providing an alternative to conventional flat foil targets. Using a high-intensity laser pulse of $6 \times 10^{20}\ \mathrm{W/cm^2}$, we demonstrate proton energies exceeding 90 MeV, which is notably higher than the energies obtained from rectangular foils of the same thickness. Achieving such energy levels is crucial for advancing practical applications. Furthermore, our results demonstrate that the target diameter plays a decisive role in influencing the acceleration process. The underlying physical mechanisms responsible for these observations are also analyzed and discussed in detail.

Keywords: Laser-plasma interaction, TNSA, PIC simulation.

PACS: 52.38.Kd, 52.38.-r, 41.75.Jv

1 Introduction

Over the past two decades, continuous advancements in high-power laser facilities have made it possible to explore the interaction of matter with extremely intense laser pulses. These interactions extend well beyond the non-relativistic regime, resulting in the generation of extremely strong electric and magnetic fields[1]. When such super-intense laser pulses strike matter, they cause almost instantaneous ionization, creating plasma. This plasma not only sustains the strong fields but also acts as a medium for producing highly energetic beams of particles[2].

Laser-driven ion sources are particularly attractive because they are compact, cost-efficient, and much easier to handle compared to conventional accelerators. Traditional accelerators achieve accelerating gradients of only a few tens of MV/m, requiring kilometre-long beamlines to reach multi-GeV ion energies. In contrast, laser–plasma accelerators can maintain accelerating gradients approaching TV/m, enabling tabletop-sized setups with tremendous potential for applications[3, 4]. At present, significant research efforts are devoted to accelerating protons and heavier ions from solid targets such as metals and plastics using intense laser pulses.

The classification of plasma is based on the electron density in relation to the critical density(n_c) as underdense ($n_e < n_c$) or overdense ($n_e > n_c$). In underdense plasmas, the refractive index remains real, allowing electromagnetic waves to propagate. In overdense plasmas, the refractive index becomes imaginary, preventing wave propagation. Thus, the choice of target and its density relative to n_c critically affects energy absorption and wave propagation.

Since the 1970s, laser–matter interaction studies have revealed efficient electron acceleration. Early experiments focused on pushing electrons to relativistic energies, while subsequent work examined how these energetic electrons could transfer energy to ions, especially protons. The first clear evidence of MeV-scale protons from laser–solid interactions came in the 1990s, with energies steadily increasing through subsequent experiments. A major breakthrough occurred in 2000 when Snavely et al. demonstrated proton beams with maximum energies of 55 MeV, sparking strong interest in the field[5].

Different mechanisms have been proposed to explain ion acceleration. Front-surface acceleration, governed by the laser's radiation pressure, can occur through hole-boring or light-sail mechanisms depending on the thickness of the target. In contrast, most experimental results can be understood using the Target Normal Sheath Acceleration(TNSA) mechanism, which is a model for rear-surface acceleration[2]. Here, hot electrons generated at the laser-irradiated surface migrate to the rear side, where the sheath field generated by the charge separation is sufficiently strong to accelerate ions to high energies. Proton beams from TNSA are typically laminar and low in emittance, though they suffer from broad energy spectra, which limits certain applications[6][7].

To maximize absorption, plasmas having electron density close to the critical density (n_c) are especially important. However, producing such near-critical plasmas is challenging. Solid targets are usually much denser than, while gas jets are far less dense. Techniques such as pre-expanding solids with secondary pulses or using cryogenic gas jets can approach near-critical conditions but often lack precise control over density profiles. Structured targets are widely investigated because they enhance laser energy absorption by both electrons and ions[8–17]. Spherical targets having diameter of a few tens of microns are also studied to accelerate ions[18–22].

In this work, we have investigated proton acceleration from a spherical target using a laser of intensity $6 \times 10^{20} W/cm^2$. The dimension of the target is selected to be smaller than the laser spot size, which has not be studied in detail in earlier works[18, 20, 21]. Manufacturing these targets have become a reality with the advancements of technology. Over the years, spherical targets have been extensively utilized in laser–matter interaction research. Spherical water droplets with micrometer-scale radii , [23, 24], gas-cluster targets having sub-micron dimensions [25, 26], and small objects supported by structures with sizes from a few hundred nanometers to several microns [19, 27] are commonly used examples of mass-limited targets. A major advancement was made by Ostermayr et al., who, for the first time, employed well-defined and truly isolated charged polystyrene (C_8H_8) spheres as targets, by levitating it using a Paul trap[28]. The composition as well as the dimension of the target used in our work are well within the range which has been tested in earlier experiments of laser matter interaction, however the study of ion acceleration using laser of intensity (I_0) in $10^{20} - 10^{21}\ W/cm^2$ range is novel. The introduction is followed by simulation parameters in section 2. Section 3 is the results and discussion and the conclusion is discussed at the end in section 4.

2 Simulation Scheme

In this work, two-dimensional particle-in-cell (PIC) simulations were conducted with the fully relativistic PIC code EPOCH[29]. The simulation grid was defined with a spatial resolution of $\Delta x = 8.5\ nm$ and $\Delta y = 13.33\ nm$. Open boundary conditions were applied to fields and particles across all boundaries of the simulation box.

The laser pulse considered in our work has central wavelength of $\lambda = 1\mu m$ with a gaussian profile. The transverse size (FWHM) of the pulse is $4.24\mu m$, while the pulse duration,τ_L is 56.5 femtoseconds (fs). The maximum intensity(I_0) of the laser is $6 \times 10^{20} W/cm^2$ corresponding to normalised amplitude $a_0 = \frac{eE}{m_e \omega c}$ = 20.8. The laser enters the simulation box from the left boundary and propagates along x-direction.

For the study, both spherical target and flat foils are considered. In case of the spherical target, the center is positioned at $x = 0$ with diameter same as the thickness of the foil. The front surface of the flat foil is positioned at $x = 0$. The transverse length along the y-direction is 8 micron. The electron density taken is $n_e = 270 n_c$, where $n_c = 1.11 \times 10^{21}/cm^3$ denotes the critical density for the laser wavelength $\lambda = 1\mu m$. The target taken in our study is composed of plastic (CH). In the simulations, 150 macroparticles per cell are employed for electrons and protons.

3 Results and discussion

As the laser is irradiated on the target surface, electrons respond first and gain momentum. The laser pulse reaches its peak at the target at approximately 80 fs of simulation time. The electron density plot at this time shows the electrons escaping into the vacuum. These electrons are accelerated due to ponderomotive force of the pulsed laser. The electrons are driven outward, away from the center of the pulse, primarily due to the strong spatial gradients in the laser electric field. Due to a linearly polarised laser, the ponderomotive force is given by the following expression:

$$\mathbf{f}_p = -\frac{e^2}{8 m_e \omega^2} \nabla \left[E_s^2(\mathbf{r})(1 + \cos 2\omega t) \right]$$

Here, e, m_e are the charge and mass of the electrons. E_s is the laser electric field and ω is the incident laser frequency. The expression also contains an oscillatory term, which generates two bunches of electrons during each laser cycle. This term originates from the magnetic component of the Lorentz force. When the laser intensity

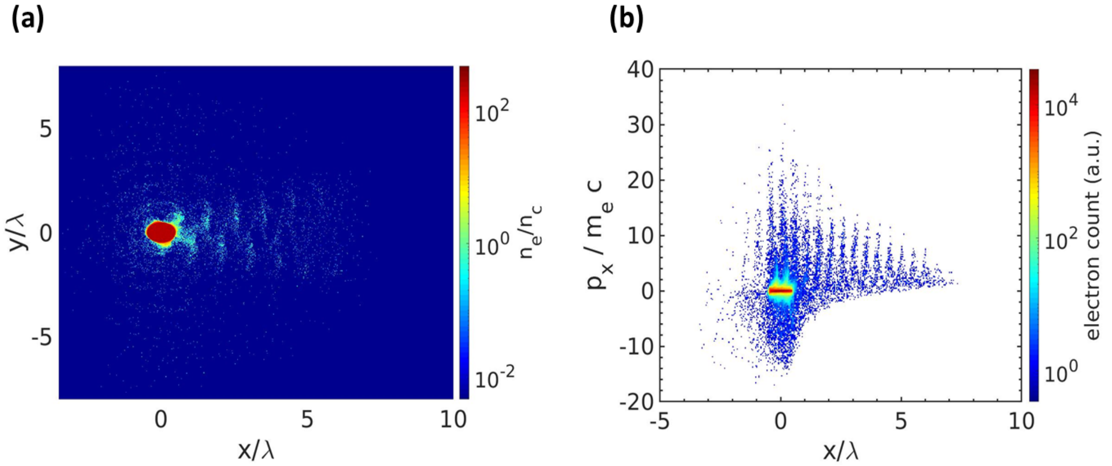

Figure 1: (a) Electron density plot at 80fs, showing electron bunches with $\lambda/2$ periodicity. (b) Corresponding electron momentum(p_x) shows the positions of bunches.

is very high ($\geq 10^{18} W/cm^2$), the effect of magnetic field part of the lorentz force generates bunches of electrons via the '$J \times B$' heating method. These bunches are spatially separated by a distance of $\lambda/2$. From the Fig. 1(a), electron bunches having spatial periodicity $\lambda/2$ are observed, which indicates the role of $J \times B$ heating in accelerating the electrons. The phase plot (Fig. 1(b)) also shows the bunches with periodicity $\lambda/2$. These highly energetic electrons or 'hot electrons' travel through the target and are trapped as they reach the rear surface. The accumulation of hot electrons at the rear surface produces a quasi-static electric field, which is strong enough to ionize and accelerate atoms from the target's rear side. This method, through which the rear ions gain momentum and accelerate is termed as Target Normal Sheath Acceleration (TNSA).

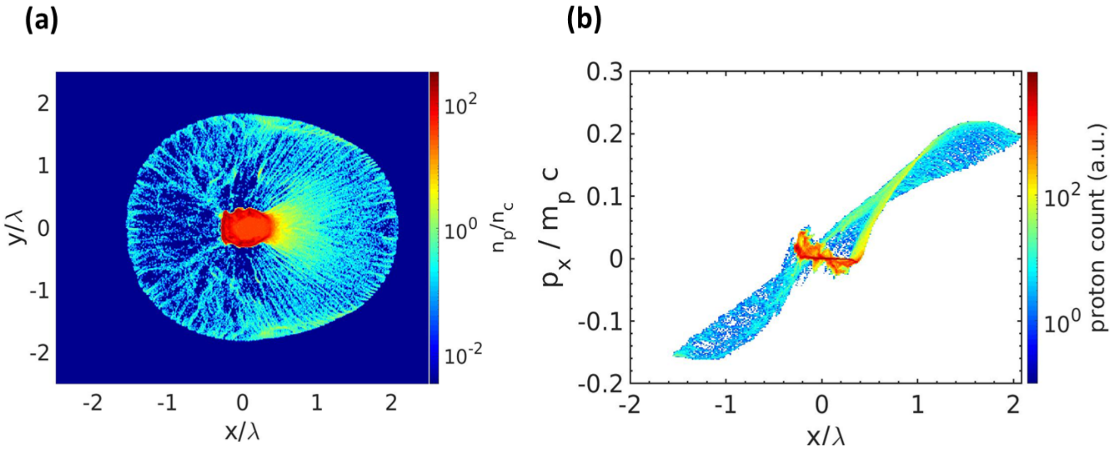

Figure 2: (a) Proton density profile at 120 fs, showing the emission of majority protons from rear surface.(b)corresponding longitudinal proton momentum profile,shows accelerated protons from both front and rear surface

The Radiation Pressure Acceleration (RPA) method is another acceleration method through the front protons gain momentum and accelerate[30]. Fig. 2(a) shows the proton density plot at around 120 fs simulation time. The protons can be seen to be accelerated from all sides of the target, however the rear protons are found to have the highest momentum(Fig. 2(b)). These protons are accelerated by TNSA mechanism. The RPA mechanism is also observed to accelerate the front protons but the momentum is much less than the TNSA accelerated rear protons. For RPA to be dominant, the intensity of the laser needs to be $\gtrsim 10^{22}\ W/cm^2$.

The simulation is performed up to a time till the energy of the protons saturate. Fig. 3(a) shows the proton density at 500 fs simulation time, which is the end of the simulation. The Fig. 3(b) presents the energy spectrum

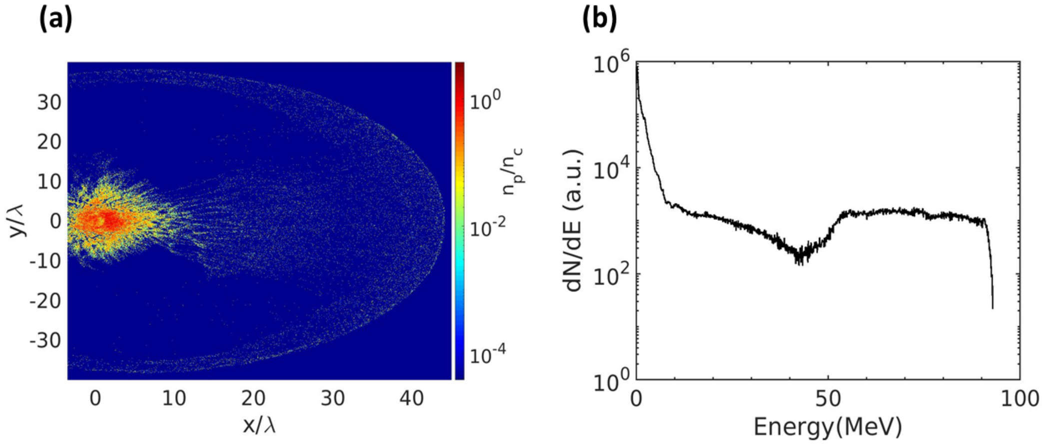

Figure 3: (a) Density plot showing accelerated protons. (b) Proton energy spectra at 500 fs. The maximum proton energy is $\sim$ 93 MeV.

of the accelerated protons measured at this time. The maximum energy of the protons is found to be around 90 MeV. This energy is significantly higher than the energy obtained from conventional flat foils of similar thickness. Protons with energy around 90 MeVs are desired for numerous practical applications. Using a flat foil with the same thickness as the spherical target's diameter results in proton energies of approximately 50 MeV. The proton energy spectra for the spherical target as well as the flat foil are shown in Fig. 4(a).

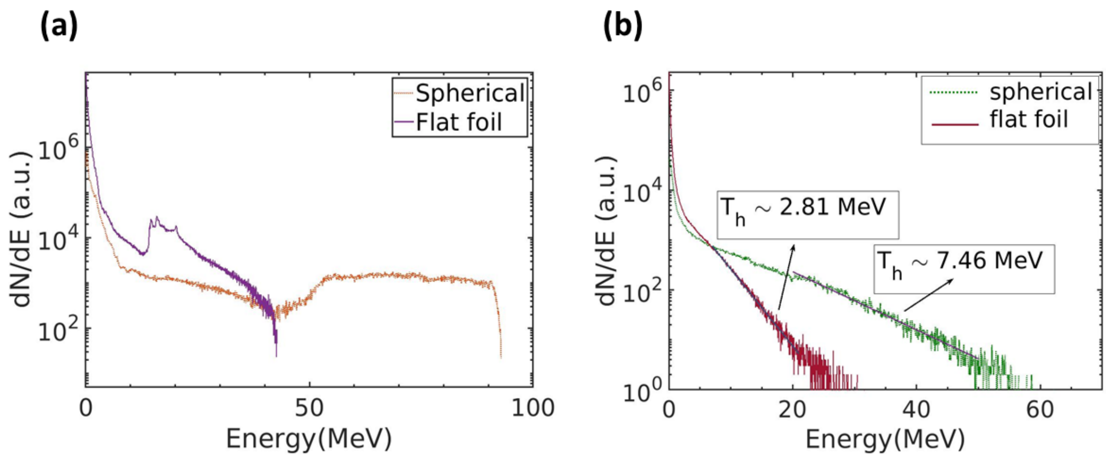

Figure 4: (a) Proton energy spectra for the foil (purple solid line) and spherical target(orange dotted line) showing spherical target has boarder and high-energetic distribution compared to flat foil at 500 fs. (b) Electron energy spectra for the foil (red solid line) and spherical target(green dotted line) showing the hot electron temperature(T_h) when electron energy is maximum. The hot electron temperature increase significantly in spherical target. Here the thickness of the foil and the sphere are same and equal to 1 micron.

With an objective of understanding the reason behind the observed higher energy in the spherical target, we have obtained the electron energy spectra and the hot-electron temperature for the two cases. The temperature of the hot electrons serves as an important indicator of how much energy the electrons have absorbed from the laser. A higher electron temperature generally means that the electrons have gained more energy, which subsequently leads to the creation of a stronger sheath electric field at the target rear surface. This field is essential for accelerating protons to high energies. From Fig. 4(b), it is evident that energy of the electrons and also the T_h is higher in the spherical target. This ultimately contributes to the higher energy in the protons in the spherical target.

The behaviour of the accelerated protons in our simulations is analyzed using the theoretical model developed by Mora et al., which quantitatively predicts proton energies in the TNSA regime.[31]. The model is a 1D collisionless plasma expansion model where electrons are treated as Boltzmanian and Ions are treated as cold and initially at rest. Electron density profile follows the Boltzmann's equation and ions are treated through fluid equations. With fluid equations and Poisson's equation, electric field is calculated at the ion front. It predicts the ion energy spectrum and ion cut off energy.

The maximum ion energy due to TNSA can be expressed as [31] [32]:

$$\varepsilon_{\text{max}} = 2Zk_BT_h\left[\ln\left(\tau' + \sqrt{\tau'+1}\right)\right]^2.$$

Here

$$\tau' = \frac{\omega_{pi}t}{\sqrt{2e_N}}, \qquad \omega_{pi} = \sqrt{\frac{e^2 n_{e0}}{\epsilon_0 m_i}},$$

is the ion plasma frequency with ion mass m_i, t the acceleration time, $e_N = 2.718...$, Z is charge state of the ion species, n_{e0} denotes ion density at initial time, k_B and ϵ_0 are the Boltzman constant and the dielctric constant in vacuum.

For sufficiently long acceleration times ($\omega_{pi}t \gg 1$), the cutoff energy can be approximated as

$$\varepsilon_{\text{max}} \approx 2Zk_BT_h\left[\ln(2\tau')\right]^2.$$

An acceleration time of $t \sim 1.3\,\tau_L$ has been found to provide a good prediction of the proton energy scaling.

From the above expressions and using the hot electron temperature obtained in our simulations, the expected maximum proton energy for a flat foil target is found to be about ~ 45 MeV. This value agrees well with the energies obtained in our simulations, demonstrating the consistency of the model in this case. On the other hand, the same model predicts a proton energy of approximately 121 MeV for the spherical target. However, this value is noticeably higher than what we actually obtained from our simulation results.

The difference arises because the theoretical model used here is essentially one-dimensional (1D). While such a model is quite suitable for describing the simpler case of a flat foil target, it may not fully capture the more complex effects introduced by curved or spherical geometries. In the case of spherical targets, the geometry strongly impacts the dynamics of the interaction and, in turn, the final energies. In particular, the hot electrons, which generate the sheath field and drive ion acceleration, behave differently in spherical geometry. Although they initially contribute to a strong accelerating field, the electrons may naturally diverge as they move away from the curved surface. This divergence weakens the sheath field over time, leading to a reduction in the strength of ion acceleration and consequently a lower maximum proton energy than predicted by the simple theory.

From the Fig. 2(b), the protons having maximum energy can be observed to be accelerated from the rear surface. The hot electron cloud at the rear surface creates a sheath electric field at the rear surface and this longitudinal field accelerates the protons from the rear surface of the target, via the TNSA mechanism. The longitudinal electric field plot is obtained for both the flat & the spherical target, as seen in Fig. 5. It can be seen that the strength of the electric field created on the rear surface of the spherical target is much stronger than the field generated in the flat foil case. The combined effect of multiple physical phenomena contribute to the enhanced strength of the electric field generated by the hot electrons. The smaller transverse size of the spherical target results in the laser energy being distributed among fewer electrons compared to an extended flat foil target. This leads to enhanced energy of the electrons. Another important reason behind the enhanced T_h is due to the fact that due to the size of the target, the diffracted part of the laser from the edges of the target creates a current of electrons across the surface, leading to an elevated count of electrons at the rear surface. This leads to the enhanced longitudinal electric field in the spherical target case. This consequently results in higher energy in the accelerated protons, which is driven by this sheath field.

In the next part of our study, we examined how the dimension of the target, when compared to that if the laser spot, influences both laser energy absorption and the subsequent acceleration of protons. Since the majority of the laser energy is concentrated in the central part of the laser, the relative dimension of the target becomes an important factor in determining how effectively the energy is absorbed and transferred to the particles. The spot size of the laser used in our study is 4.24 micron.

Simulation are performed by varying the target diameter systematically from 0.8 microns to 3 microns. The proton cutoff energy is obtained from the spectra for different diameters and is shown in Fig. 6(a). The findings indicate that larger target diameters correspond to lower maximum proton energies. This behaviour highlights the strong influence of target size on the efficiency of proton acceleration. The dependence of proton cutoff energy on

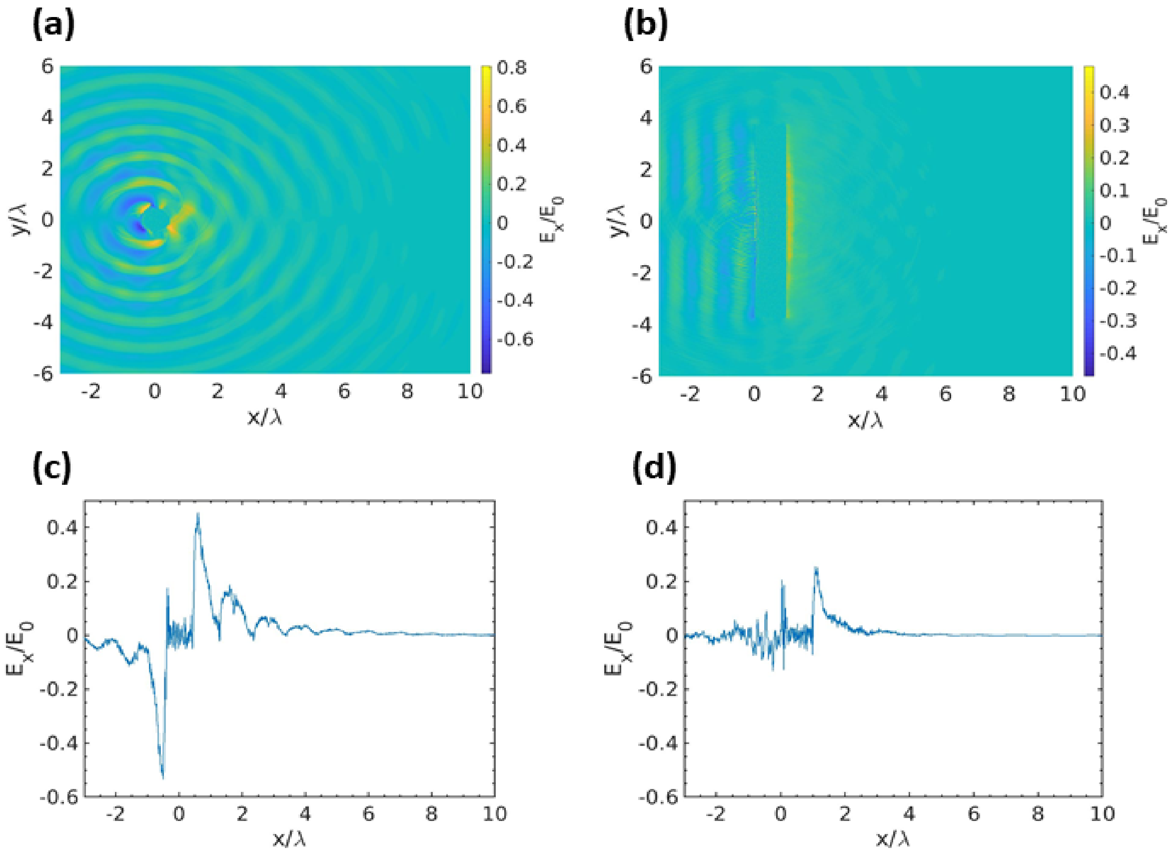

Figure 5: (a) Longitudinal electric field (E_x/E_0) profile in the spherical target. (b) E_x/E_0 plot in the x-y plane in the flat foil.(c) E_x/E_0 plot close to the central axis (y=0) for the flat foil.(d) Electric field plot close to the center of the target (y=0) for the flat foil. The plots shown are from 100 fs of simulation time, when the laser interaction with the target has occurred and the rear sheath field is fully formed. All these plots shows the sheath field formed in the spherical target is much stronger than the field in the flat foil target case.

the diameter of the sphere is shown in Fig. 6a. For a 3 micron diameter target, the energy of accelerated proton reaches $\sim$ 50 MeV. It increases to $\sim$ 93 MeV for a 1 Micron diameter target and no significant change is observed on further decreasing the diameter to 0.8 micron. The diameter has not been decreases further below 0.8 micron.

In order to understand the reason behind the observed variation, the laser energy absorption percentage and hot-electron temperatures are obtained using the electron energy plot. The hot-electrons contribute to the formation of strong sheath electric field which drives ion acceleration from the rear surface of the target. Fig. 6(b) shows the variation of T_h with varying target diameters. The electrons temperatures are found to show a trend similar to the one observed in proton energy. The temperatures decrease with increase in diameter. The maximum T_h of $\sim$7.5 MeV is obtained for the 1 micron diameter sphere. A small decrease in the temperature is observed in the 0.8 micron case.

The hot-electron temperature variation and the variation in the laser energy absorption by the electrons can help us understand the observed variation in the proton energy. When the target diameter becomes much smaller than the size of the laser spot, a portion of the laser beam passes around the target edges without interacting with it, leading to a loss of laser energy. This effect explains the relatively higher energy absorption observed for the 3-micron diameter case and the subsequent reduction in absorption as the target diameter decreases further. However, to understand the reason behind hot electron temperature increase with decreasing target diameter up to 0.8 micron requires a detailed analysis.

Most of the energy of the laser is concentrated in the central part of the pulse. With reduction in size of the target, this concentrated energy is distributed among a smaller number of particles within the interaction region. Consequently, each particle receives a larger share of the absorbed energy, which results in an overall enhancement

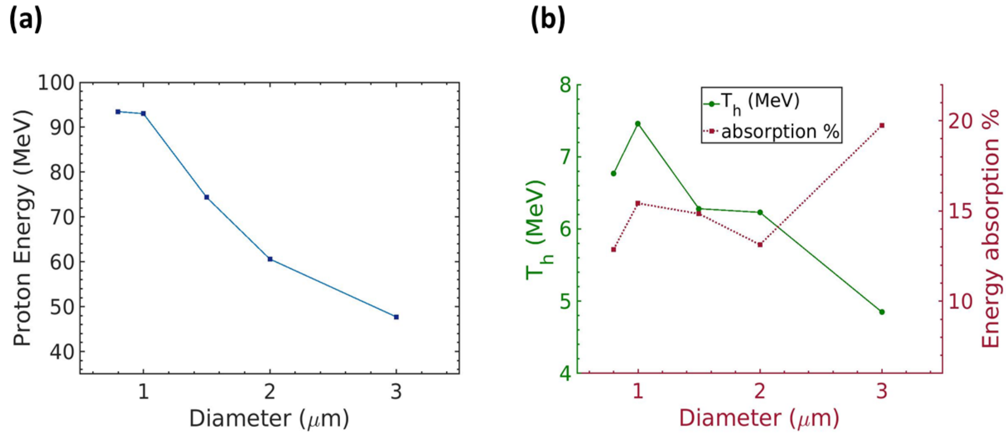

Figure 6: (a)The plot shows variation of proton cutoff energy with target diameter. Proton energy decreases as the target diameter increases. (b) This plot shows variation of hot electron temperature (T_h) and laser energy absorption on target diameter. The hot electron temperature decreases with increasing diameter while the energy absorption exhibits an increasing trend.

in the energy of the hot electrons. Elevated hot electron temperatures enhance the rear-surface sheath field strength, consequently improving the efficiency of proton acceleration.

4 Conclusion

This work explores the acceleration of protons from spherical targets, with particular emphasis on the underlying mechanisms driving ion generation and energy gain. While flat foils have been the standard choice for many years, our results show that spherical targets provide advantages that can significantly improve ion acceleration. Most of the previous studies were limited to studying electron and ion acceleration from targets with diameter greater than the laser spot size and with low intensity lasers, our investigation focuses on targets with diameter less than the laser spot size[18–21]. Isolated spherical targets can now be manufactured for various studied[20]. In our study, a spherical target of diameter 1 μm is found to provide proton cutoff energy of 93 MeV, whereas the flat foil of equal thickness produces 45 MeV. This demonstrates a substantial enhancement in energy when using a curved geometry. Similarly, the T_h in the spherical target is found to be 7.46 MeV, notably higher than the 2.81 MeV obtained for the flat foil. These results confirm that spherical targets are more effective in confining electrons and generating stronger accelerating fields. We have also studied the effect of varying the diameter of spherical targets. The results show a decreasing trend in both maximum proton energy and hot electron temperature with increasing diameter. These ions are found to be accelerated using the TNSA mechanism. The generation of hot electrons at the front surface leads to the formation of a sheath field, enabling ion acceleration from the rear surface. It is important to note that 3D simulations generally provide more accurate predictions of experimental outcomes than 2D simulations, although they require significantly greater computational resources. In order to qualitatively comprehend the physical process and mechanism involved during laser-plasma interaction, 2D simulations are found to be reliable. In the context of TNSA process, although the 2D simulation usually overestimates the strength of the fields generated and the energy of the accelerated protons, the difference in the energy of protons from 2D and 3D simulations are very small[7, 33, 34]. 3D simulations are necessary to get a good idea of the expected energy in an experiment. In summary, we have shown that spherical targets provide a clear geometric advantage in laser-driven ion acceleration, offering higher particle energies and stronger electron heating. This makes them a promising candidate for applications requiring compact, high-quality proton beams.

Acknowledgement

Author Jubaraj Choudhury acknowledges financial support from the DST-INSPIRE Fellowship (No. IF190925). Support from the Core Research Grant (SERB-DST), Government of India, is also gratefully acknowledged.

References

[1] H. Daido, M. Nishiuchi, and A. S. Pirozhkov, Rep. Prog. Phys. **75**, 056401 (2012).

[2] A. Macchi, M. Borghesi, and M. Passoni, Rev. Mod. Phys. **85**, 751 (2013).

[3] V. Malka, S. Fritzler, E. Lefebvre, M.-M. Aleonard, F. Burgy, J.-P. Chambaret, J.-F. Chemin, K. Krushelnick, G. Malka, S. Mangles, *et al.*, Science **298**, 1596 (2002).

[4] E. Esarey, P. Sprangle, J. Krall, and A. Ting, IEEE Trans. Plasma Sci. **24**, 252 (1996).

[5] R. Snavely, M. Key, S. Hatchett, T. Cowan, M. Roth, T. Phillips, M. Stoyer, E. Henry, T. Sangster, M. Singh, *et al.*, Phys. Rev. Lett. **85**, 2945 (2000).

[6] S. Wilks, A. Langdon, T. Cowan, M. Roth, M. Singh, S. Hatchett, M. Key, D. Pennington, A. MacKinnon, and R. Snavely, Phys. Plasmas **8**, 542 (2001).

[7] H. Ruhl, S. Bulanov, T. Cowan, T. Lisekina, P. Nickles, F. Pegoraro, M. Roth, and W. Sandner, Plasma Phys. Rep. **27**, 363 (2001).

[8] M. Bailly-Grandvaux, D. Kawahito, C. Mcguffey, J. Strehlow, B. Edghill, M. Wei, N. Alexander, A. Haid, C. Brabetz, V. Bagnoud, *et al.*, Phys. Rev. E **102**, 021201 (2020).

[9] H. Deng, R. Sha, L. Hu, X. Jiang, N. Zhao, D. Zou, T. Yu, and F. Shao, Plasma Phys. Control. Fusion **64**, 085004 (2022).

[10] B. Feng, L. Ji, B. Shen, X. Geng, Z. Guo, Q. Yu, T. Xu, and L. Zhang, Phys. Plasmas **25**, 103109 (2018).

[11] C. Qin, H. Zhang, S. Li, N. Wang, A. Li, L. Fan, X. Lu, J. Li, R. Xu, C. Wang, *et al.*, Commun. Phys. **5**, 124 (2022).

[12] S. Chen, T. Iwawaki, K. Morita, P. Antici, S. Baton, F. Filippi, H. Habara, M. Nakatsutsumi, P. Nicolaï, W. Nazarov, *et al.*, Sci. Rep. **6**, 1 (2016).

[13] A. Sgattoni, P. Londrillo, A. Macchi, and M. Passoni, Phys. Rev. E **85**, 036405 (2012).

[14] M. Dozières, G. Petrov, P. Forestier-Colleoni, P. Campbell, K. Krushelnick, A. Maksimchuk, C. McGuffey, V. Kaymak, A. Pukhov, M. Capeluto, *et al.*, Plasma Phys. Control. Fusion **61**, 065016 (2019).

[15] G. Gadea, A. Morata, J. Santos, D. Dávila, C. Calaza, M. Salleras, L. Fonseca, and A. Tarancón, Nanotechnology **26**, 195302 (2015).

[16] A. Andreev, K. Platonov, J. Braenzel, A. Lübcke, S. Das, H. Messaoudi, R. Grunwald, C. Gray, E. McGlynn, and M. Schnürer, Plasma Phys. Control. Fusion **58**, 014038 (2015).

[17] O. Klimo, J. Psikal, J. Limpouch, J. Proska, F. Novotny, T. Ceccotti, V. Floquet, and S. Kawata, New J. Phys. **13**, 053028 (2011).

[18] J. Limpouch, J. Psikal, A. Andreev, K. Y. Platonov, and S. Kawata, Laser Part. Beams **26**, 225 (2008).

[19] A. Henig, D. Kiefer, M. Geissler, S. G. Rykovanov, R. Ramis, R. Hörlein, J. Osterhoff, Z. Major, L. Veisz, S. Karsch, *et al.*, Phys. Rev. Lett. **102**, 095002 (2009).

[20] T. Sokollik, T. Paasch-Colberg, K. Gorling, U. Eichmann, M. Schnürer, S. Steinke, P. Nickles, A. Andreev, and W. Sandner, New J. Phys. **12**, 113013 (2010).

[21] A. Kemp and H. Ruhl, Phys. Plasmas **12** (2005).

[22] T. Liseykina, S. Pirner, and D. Bauer, Phys. Rev. Lett. **104**, 095002 (2010).

[23] T. Sokollik, M. Schnürer, S. Steinke, P. Nickles, W. Sandner, M. Amin, T. Toncian, O. Willi, and A. Andreev, Phys. Rev. Lett. **103**, 135003 (2009).

[24] S. Karsch, S. Düsterer, H. Schwoerer, F. Ewald, D. Habs, M. Hegelich, G. Pretzler, A. Pukhov, K. Witte, and R. Sauerbrey, Phys. Rev. Lett. **91**, 015001 (2003).

[25] S. Ter-Avetisyan, B. Ramakrishna, R. Prasad, M. Borghesi, P. Nickles, S. Steinke, M. Schnürer, K. Popov, L. Ramunno, N. Zmitrenko, *et al.*, Phys. Plasmas **19**, 073112 (2012).

[26] Y. Fukuda, A. Y. Faenov, M. Tampo, T. Pikuz, T. Nakamura, M. Kando, Y. Hayashi, A. Yogo, H. Sakaki, T. Kameshima, *et al.*, Phys. Rev. Lett. **103**, 165002 (2009).

[27] K. Zeil, J. Metzkes, T. Kluge, M. Bussmann, T. Cowan, S. Kraft, R. Sauerbrey, B. Schmidt, M. Zier, and U. Schramm, Plasma Phys. Control. Fusion **56**, 084004 (2014).

[28] T. M. Ostermayr, D. Haffa, P. Hilz, V. Pauw, K. Allinger, K.-U. Bamberg, P. Böhl, C. Bömer, P. Bolton, F. Deutschmann, *et al.*, Phys. Rev. E **94**, 033208 (2016).

[29] T. Arber, K. Bennett, C. Brady, A. Lawrence-Douglas, M. Ramsay, N. Sircombe, P. Gillies, R. Evans, H. Schmitz, A. Bell, *et al.*, Plasma Phys.Control. Fusion **57**, 113001 (2015).

[30] E. Clark, K. Krushelnick, J. Davies, M. Zepf, M. Tatarakis, F. Beg, A. Machacek, P. Norreys, M. Santala, I. Watts, *et al.*, Phys. Rev. Lett. **84**, 670 (2000).

[31] P. Mora, Phys. Rev. Lett. **90**, 185002 (2003).

[32] J. Fuchs, P. Antici, E. d'Humières, E. Lefebvre, M. Borghesi, E. Brambrink, C. Cecchetti, M. Kaluza, V. Malka, M. Manclossi, *et al.*, Nature Phys. **2**, 48 (2006).

[33] L. A. Daneshmand, M. Aszalos, S. Feister, and J. R. Smith, Phys. Plasmas **32** (2025).

[34] L. Fedeli, A. Formenti, L. Cialfi, A. Pazzaglia, and M. Passoni, Sci. Rep. **8**, 1 (2018).